Peer-Reviewed Technical Communication

A Framework for Acoustic Segmentation Using Order Statistic-Constant False Alarm Rate in Two Dimensions From Sidescan Sonar Data

Sebastián A. Villar, *Member, IEEE*, Mariano De Paula, Franco J. Solari, and Gerardo G. Acosta, *Senior Member, IEEE*

***Abstract*—This paper describes a framework for object segmentation from sidescan sonar acoustic data. The current techniques consume a great deal of computational resources to accurately carry out object segmentation. They also involve the tuning of many parameters to obtain good quality images. This is due to the handling of the large data volume generated by these devices and environmental fluctuations such as salinity, density, temperature, and others variations. The framework proposed uses a migration and adaptation of a technique widely used in radar technology for detecting moving objects. This radar technique is known as order statistic-constant false alarm rate (OS-CFAR) applied in 2-D. OS-CFAR 2-D rank orders the samples obtained from a sliding window to make a segmentation of the image. This segmentation is done into several types of regions: acoustic highlight, shadow, and different seafloor reverberation areas. OS-CFAR 2-D is less sensitive than other methods to the presence of the speckle noise due to the use of order statistics. This proposal was contrasted experimentally on real images. Likewise, an experimental comparison with the results obtained with the undecimated discrete wavelet transform, active contours, Markov random field, and accumulated cell averaging CFAR applied in two dimensions technique is also presented.**

***Index Terms*—Image segmentation, order statistic-constant false alarm rate (OS-CFAR), sidescan sonar (SSS), sonar imagery.**

I. Introduction

ACOUSTICAL data may provide high-resolution images of underwater areas, and they are particularly useful in waters with low transparency for optical waves [1]. Hence, sonars are relevant sensors for several practical applications, such as marine geology, commercial fishing, underwater archeology, resources search, extraction and oil drilling, inspection and maintenance of pipelines, mine or waste detection, and other types of monitoring [2], [3]. In this sense, a sidescan sonar (SSS) is an effective tool for high-resolution mapping of the seabed due to the maturity of its technology and an excellent cost/quality tradeoff [2].

SSS uses linear arrays of transducers on the port and starboard sides, emitting and receiving in phase with one to another, or in a controlled phase relationship. Acquired data are projected on a line traced in the across-track direction. This scanning line is called beam and each beam value is known as bin, representing acoustic reverberation power. Thus, an SSS acoustic image is achieved by placing a sequence of consecutive beams in along-track direction to describe the seafloor in 2-D. For further details, refer to [2], [4], and [5].

These devices have been proved in deep waters with very satisfactory results [3], [6]–[10]. However, they need an extra amount of postprocessing of acoustical data to obtain a useful image. Typically, in SSS high-resolution images, three types of regions are identified: highlight, shadow, and seafloor reverberation areas [11]. Separation in regions is a typical process known as segmentation and it is the bottleneck of the postprocessing computational effort. The implementation of the segmentation process exploits the fact that the objects located on the seafloor are more reflective than the surrounding sediment. The acoustic highlight considerably varies according to the relative sonar orientation with regards to the target. Likewise, objects, which stand out above the seafloor, generate shadows. The shadow length depends on the object's upright height to the seafloor. Given that data collection is performed from a moving vehicle, the sonar geometry to the target is variable. Therefore, a shadow may be present even when acoustic highlight is not. The seafloor reverberation area is complex because it contains a noise known as speckle [1]. Generally, this noise is present in all imaging systems with coherent illumination. Speckle noise renders ineffective the segmentation schemes of the digital image processing theory [12]. Thus, the ability to segment high-resolution acoustical images in an efficient and robust way is essential for any practical application.

Many approaches to acoustic image segmentation are currently available. They can be categorized as supervised or unsupervised. Supervised algorithms use a classifier trained for region segmentation [13]–[15]. On the other hand, unsupervised methods perform segmentation through a direct analysis of the input image without any *a priori* information. Considering both types of algorithms, we can mention the following: Multifractal analysis [16], Markov random field (MRF) [17], [18], local fourier histograms [19], active contours (AC) [20], Gauss–Markov random field model [11], undecimated discrete wavelet transform (UDWT) [1], [21], among others. These algorithms require either a learning stage to automate their processes or computationally expensive mathematics models to segment an image in a predefined number of regions.

All of these approaches to segmentation vary in the final quality of the acoustic image. This quality is related to features such as speed, efficiency, resource requirements, accuracy, and robustness of the postprocessing algorithm. The quality can be quantified through a comparison with manual segmentation by an expert [1]. According to the application, one feature is more important than other. For instance, in the perception system of an autonomous underwater vehicle (AUV), the online feature is prioritized. That is, speed and robustness are more important than accuracy. There is always a tradeoff between accuracy and computer effort for these algorithms. In [4], an approach was

Manuscript received July 5, 2016; revised December 16, 2016, May 22, 2017, and June 17, 2017; accepted June 22, 2017. *(Corresponding author: Sebastián A. Villar.)*

Associate Editor: A. Trucco.

The authors are with the Engineering Group INTELYMEC, Argentinean National Research Council, National Buenos Aires Province Centre University, Olavarria 7400, Argentina (e-mail: svillar@fio.unicen.edu.ar; mariano.depaula@fio.unicen.edu.ar; fjsolari@fio.unicen.edu.ar; gerardo.acosta@ieee.org).

Digital Object Identifier 10.1109/JOE.2017.2721058

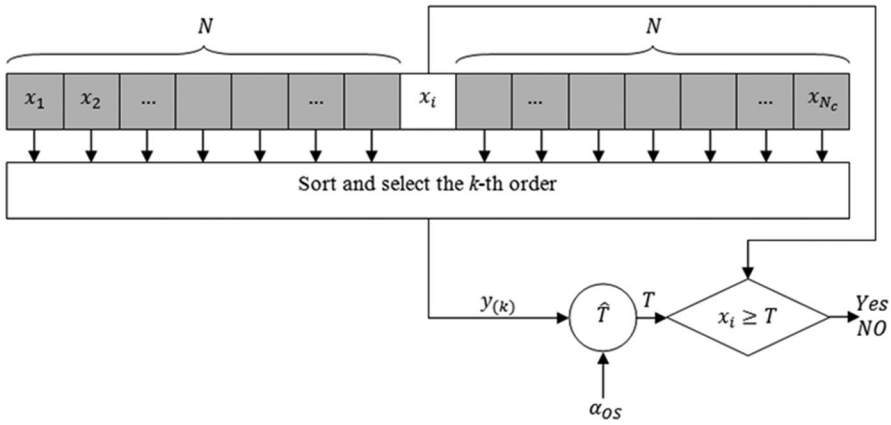

Fig. 1. Generic architecture of the OS-CFAR 1-D process.

presented for such applications. However, when accuracy is needed in applications such as seabed classification, a more complex, computer effort demanding, algorithm is needed, and even further, classification may need to be done over the final mosaic obtained from several image [22]. In this direction, this paper proposes a framework for sonar imagery acoustic segmentation that improves quality at the expense of increasing a little bit the processing time. In this paper, we resort to the techniques known as constant false alarm rate (CFAR) [23] with regards to the noise power to make segmentation and then obtain the detections.

The framework presented in this paper uses a technique known in radar technology as rank-based or order statistics-constant false alarm rate (OS-CFAR) applied in 2-D [24], [25]. It represents a detection technique to obtain estimates of the signal to clutter ratio at each range increment [25], [26]. This technique is less sensitive than other CFAR methods to the presence of multiple targets and to nonhomogeneous clutter distributions in the reference window [27]. OS-CFAR 2-D applied in sonar technology reduces the speckle noise due to the bins order to estimate the adaptive threshold. Furthermore, as it will be demonstrated, OS-CFAR 2-D is able to perform an accurate and robust acoustic segmentation through low computational resources consumption and the need of a small set of a few parameters for its application.

This paper is organized as follows. Section II discusses the basic concepts about OS-CFAR 1-D radar target detection. Section III describes the proposed framework for acoustic image segmentation adapting the OS-CFAR 2-D technique. Section IV shows a comparison of this framework with the results obtained from UDWT [1], AC [20], accumulated cell averaging CFAR applied in two dimensions (ACA-CFAR 2-D) [4], and MRF [17], [18] segmentation techniques. Finally, Section V presents the conclusion.

II. Radar Target Detection Using Order Statistics-Constant False Alarm Rate in 1-D

The detection problem in radar technology consists of analyzing any radar sample with the purpose of detecting the presence or absence of a target. Detection is usually done through the contextual information analysis of each sample. In [23], two hypotheses were defined for this analysis: 1) the sample is the background (H_0), and 2) the sample is a combination of interference and echoes of a target (H_1). If the detection system decides that H_0 is validated (target is not present), then hypothesis H_0 is stated. Otherwise, if the detection system decides that H_1 is validated, then hypothesis H_1 is stated, meaning that the target is present.

Fig. 1 shows a generic architecture of the OS-CFAR 1-D process [23] applied on a row vector of $1 \times N_c$ samples. Each cell contains an interference power value β^2. This is a real positive quantity and this is the reason why it is represented by the squared value β^2. The central cell x_i is called the cell under test and is examined in the detection process. The total number of cells N_c around the cell under test x_i (including the cell under test) is calculated using

$$N_c = 2N + 1 \tag{1}$$

where N represents the number of reference cells and $2N$ the total number of neighboring cells.

OS-CFAR rank orders the interference power values $\{x_1, x_2, \ldots, x_{N_c}\}$ to form a new sequence in ascending numerical order denoted by $\{x_{(1)}, x_{(2)}, \ldots, x_{N_c}\}$. The *k*th element of the ordered list is called the *k*th-order statistic. In OS-CFAR, the *k*th value is selected as representative of the interference level and threshold $\hat{T}$ is set applying a multiplier or scale factor α_{OS}

$$\hat{T} = \alpha_{OS}\ x_{(k)}. \tag{2}$$

This multiplier α_{OS} is a constant value determined from false alarm probability P_{fa}. As OS-CFAR keeps on a constant false alarm probability, the detection threshold of (2) only varies depending on $x_{(k)}$ value. Therefore, this technique considers the contextual information of each cell under test to determine an adaptive detection threshold.

In [28], it is indicated that if the noise is exponentially distributed, then OS-CFAR does not depend on the interference power value β^2. Besides, the alpha multiplier α_{OS} is required to get the specified P_{fa}. In [23], the notation is simplified to determine the P_{fa} from three parameters (k, N_c, and α_{OS}) as follows:

$$P_{fa} = k \binom{N_c}{k} \frac{\Gamma(\alpha_{OS} + N_c - k + 1)\,\Gamma(k)}{\Gamma(\alpha_{OS} + N_c + 1)} \tag{3}$$

where $\Gamma(\cdot)$ is the gamma function. From (3), using integer values for α_{OS} and selecting gamma function $\Gamma(n) = (n-1)!$, the false alarm probability can be computed by

$$P_{fa} = \frac{N_c!\,(\alpha_{OS} + N_c - k)!}{(N_c - k)!\,(\alpha_{OS} + N_c)!} \quad [\alpha_{OS} \text{ integer}]. \tag{4}$$

As Nathanson *et al.* suggests in [29], the statistical order k[1] for OS-CFAR technique should be $0.75N_c$ or higher ($0.833N_c$ or $0.875N_c$

[1]Note that the statistical order *k* must be an integer value, and therefore, it must be rounded to the nearest integer.

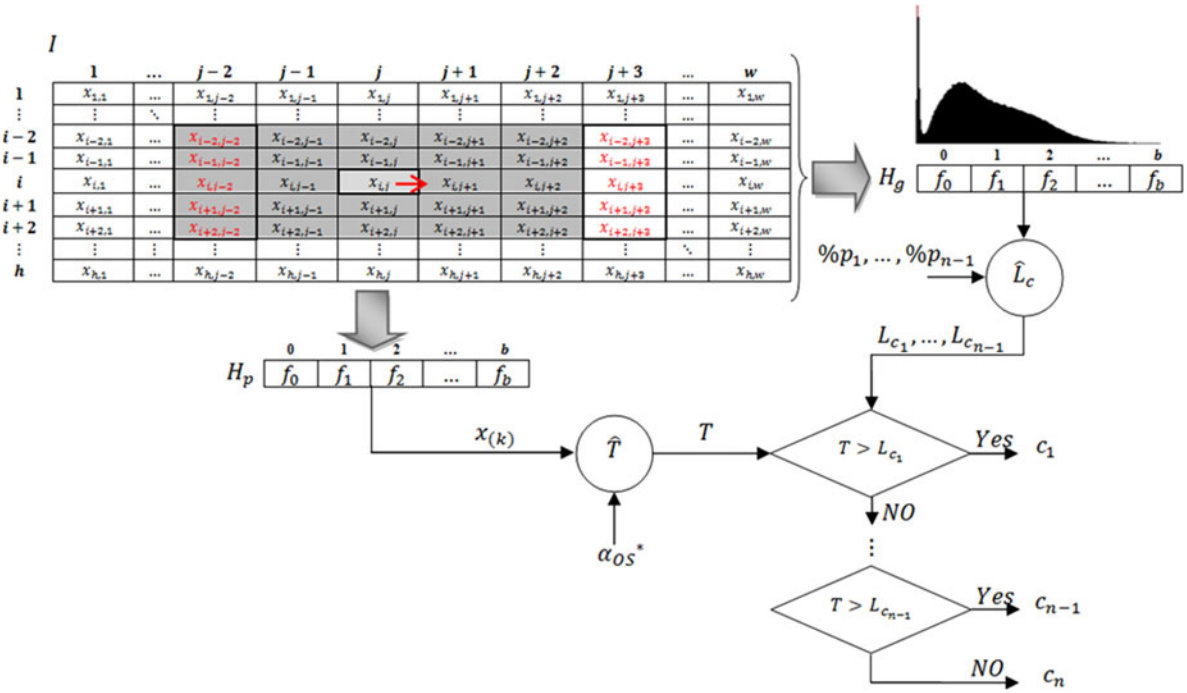

Fig. 2. General framework for acoustical segmentation using OS-CFAR 2-D.

are also typical values to use [25]). In other words, the selected value for the estimated threshold should exceed three quarters of the window samples. Using (4), depending on only two variables (N_c and α_{OS}), the following is obtained:

$$P_{fa} = \frac{N_c!\,(\alpha_{OS} + 0.25N_c)!}{0.25N_c!\,(\alpha_{OS} + N_c)!} \quad [\alpha_{OS} \text{ integer}]\,. \tag{5}$$

III. Framework for Acoustic Image Segmentation Using Order Statistics-Constant False Alarm Rate in 2-D

This section proposes a general framework that adapts and migrates the basic OS-CFAR 1-D concepts in radar technology (see Section II) to acoustical environment technology. To carry out this adaptation, different modifications are necessary. They will be explained as follows: OS-CFAR technique extension to 2-D (see Section III-A); application of efficient rank-order strategies to reduce computational resources (see Section III-B); and extension to multiclass segmentation (see Section III-C). In the acoustical domain, radar interference power is interpreted as digitized acoustical reverberation power. For an acoustical image I of size $h \times w$ (height $\times$ width), each digitized acoustical reverberation power is represented with a relative cell value to a spatial coordinate (i, j). Refer to Fig. 2, where the general framework for acoustical segmentation using OS-CFAR 2-D is shown. Before applying the acoustical segmentation process to an SSS image, it is generally necessary to make some geometrical corrections (i.e., slant range correction and anamorphosis) and radiometric correction (i.e., across-track and along-track correction) [2], [5], [30], [31]. The SSS acoustic images are prone to have numerous perturbations, geometrical and natural, which interfere in the segmentation process [9]. The movement of sonar device affects the relative position of features in the acoustic image and its true location in the seafloor. For instance, the relative orientation of the pipeline and its real position is a fundamental system requirement.

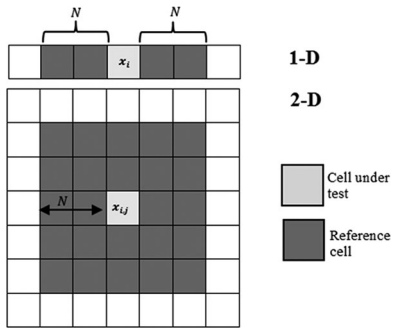

Fig. 3. Generic OS-CFAR windows for 1-D and 2-D, with $N = 2$ reference cells. The total numbers of cells are $N_c = 5$ for 1-D and $N_c = 25$ for 2-D.

A. Order Statistics-Constant False Alarm Rate Extension to 2-D

OS-CFAR extension to 2-D requires implementing a sliding window or kernel that moves over the entire acoustical image. This sliding window consists in a square matrix of size $r \times r$ and distance N to the kernel center, (where N is the number of reference cells), as it is introduced in [4], [23], and [32].

Fig. 2 shows a sliding window (dark gray cells) with its center in the cell under test $x_{i,j}$ (light gray cell). The size of this kernel radius is $r = 5$ ($N = 2$) and, therefore, it contain $N_c = 25$ cells. The calculation of the total number of cells according to the reference cells for each estimation is obtained as follows:

$$N_c = (2N + 1)^2. \tag{6}$$

Fig. 3 compares two windows, one in 1-D and another in 2-D. In this example, there are the same number of reference cells than that in Fig. 2, providing a total of $N_c = 5$ for 1-D and $N_c = 25$ for 2-D, based on (1) and (6). The extension to 2-D offers more contextual information to estimate the threshold T.

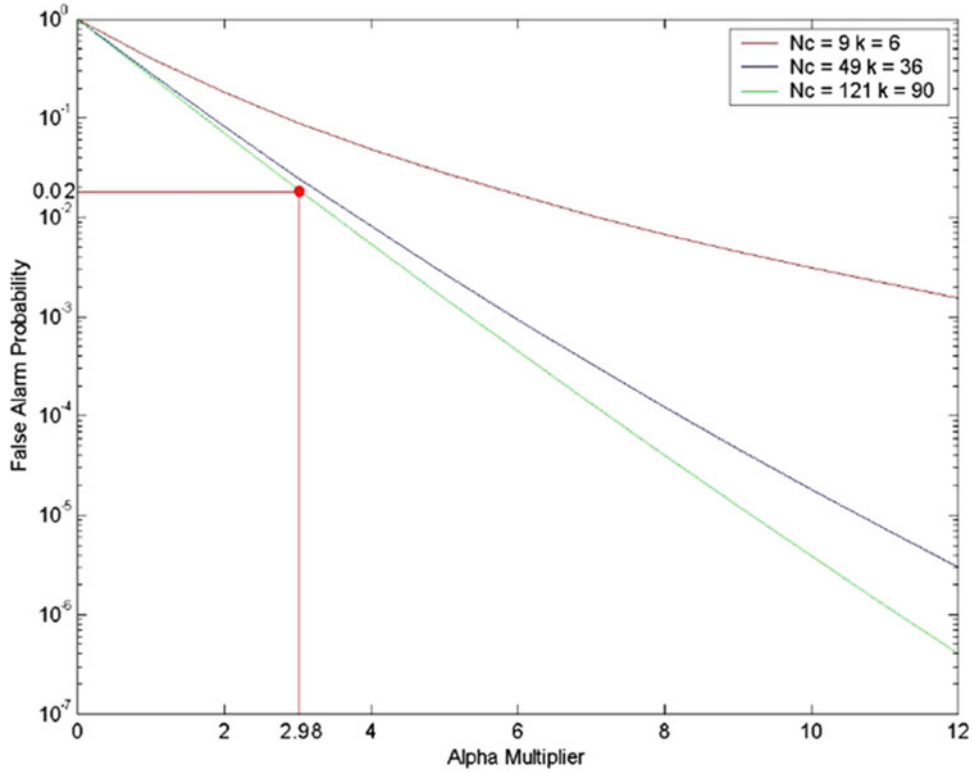

Fig. 4. Relation between false alarm probability (P_{fa}) and alpha multiplier (α_{OS}).

Note that the size of the sliding window depends on the specific problem to solve and on the acoustical image resolution provided by the acoustical device. This represents a tradeoff situation between a desired result and the processing time.

B. Application of Efficient Rank-Order Strategies

OS-CFAR 2-D implementation requires applying a rank order to the N_c digitized samples for each cell under test $x_{i,j}$ to estimate the threshold T (see Fig. 2). This sorting process involves high computational resources, being the bottleneck of the OS-CFAR 2-D method. There are different sorting methods [33], which generally vary in algorithmic complexity per cell under test. For instance, the bubble sort method complexity for worst-case performance is quadratic $O({N_c}^2)$ per cell under test (where N_c is the total number of cells being sorted), thereby OS-CFAR 2-D algorithmic complexity is the same. Note that the complexity is computed per cell under test [however, if the bubble sort method was applied to an image of, e.g., $h \times w$ (height $\times$ width), it can be shown that its global complexity would be in fact of $O(h \times w \times {N_c}^2)$].

An efficient sorting alternative is utilized the Huang classic method [34]. This method is commonly used to calculate the statistical median ($k = 0.5N_c$ order statistic) to remove different types of noise [35], [36]. In this work, the Huang method is applied using a different order statistics $k = 0.75N_c$ or higher [29]. Note that this efficient alternative presents an $O(r)$ algorithmic complexity per cell (where r is the sliding windows radius).

The Huang method uses a partial kernel histogram H_p of size $1 \times b$, where b denotes the image bit-depth (with $b = 2^{\text{image bit}-\text{depth}}$, the number of scale levels), e.g., for a 8 bits cells, the variable b has a 256 size. The partial kernel histogram stores frequencies $f_1, \ldots, f_b$ of repeatability of acoustic reverberation power values from the current window (see Fig. 2). The histogram H_p contains all neighboring cells values centered in the cell under test $x_{i,j}$ (dark gray cells). The sliding window has a size of $N_c = 25$ ($N = 2$); therefore, the histogram contains 25 values in total.

The order statistic $x_{(k)}$ is computed by mean of accumulating histogram frequencies from 0 to b and stopping when the cumulative sum is reached. In this paper, the cumulative sum must exceed $0.75N_c$. Note that other quintile or percentile can be calculated in the same way modifying this cumulative sum.

Huang method's efficiency is achieved because only a part of the histogram H_p is modified when the sliding window displaces. Fig. 2 shows an example where the window center shifts one pixel to the right, e.g., from $x_{i,j}$ to $x_{i,j+1}$. Then updating H_p requires removing those values from $x_{i-2,j-2}, \ldots, x_{i+2,j-2}$ and adding them to $x_{i-2,j+2}, \ldots, x_{i+2,j+2}$. Thus, $2N + 1$ removals and $2N + 1$ additions need to be carried out to update the kernel histogram. In this way, histogram H_p is updated to calculate the new statistic order $x_{(k)}$ for the new cell under test $x_{i,j+1}$ used to estimate the threshold T. Thus, the method's algorithmic complexity per under test cell is $O(r)$.

To estimate the threshold *T,* it is also necessary to compute α_{OS}. This may be done resorting to (3) or to (4). It was decided to use this approach to obtain α_{OS} from P_{fa}, N_c, and k using a linear interpolation of the integer values of (4), once the P_{fa} was selected, according to the segmentation performance obtained. This approach is depicted in Fig. 4, taking, as an example, three different sliding windows choices with N_c: 9 (red line), 49 (blue line), and 121 (green line). Likewise, the statistics order k utilized for $0.75N_c$ is 6, 36, and 90, respectively. The red dot shows a $P_{fa} = 0.02$, $N_c = 121$ ($N = 5$) cells, and order statistics $k = 90$, the alpha multiplier value will shed a $\alpha_{OS} = 2.98$.

Note that if the P_{fa} decreases, then α_{OS} increases, and therefore, threshold T will be amplified, increasing the separation among different types of region and the noise filtering feature. On the other hand, if P_{fa} increases, then α_{OS} decreases and threshold T will be attenuated.

C. Multiclass Segmentation

In the standard OS-CFAR version (see Section II), the estimated detection threshold is compared with the cell under test to determine whether the target is present or not. In the proposed framework, it is the estimated detection threshold that is used to segment the predefined types of regions (see Fig. 2). This provides a filtered cell value decreasing speckle noise, as it has been experimentally demonstrated. Thereby, this output T is compared to the limits $L_{c_1}, \ldots, L_{c_{n-1}}$ to segment a finite group of *n* regions $c_1, \ldots, c_n$. According to the literature, in acoustical imagery, segmentation can be binary or ternary. When it is binary, it distinguishes two classes of regions: acoustic highlight (c_1) and seafloor (c_2). When it is ternary, it distinguishes a third class known as acoustic shadow (c_3). Anyways, the proposed framework can be extended to the segmentation of n regions.

In the first step to estimate the segmentation limits, it is needed to calculate a global histogram H_g (size $1 \times b$, where b denotes the image bit depth) with frequencies $f_1, \ldots, f_b$ of repeatability of the acoustical reverberation power values. This global histogram H_g represents a global description of the acoustical image, offering useful information to determine separation limits. Even when these limits $L_{c_1}, \ldots, L_{c_{n-1}}$ can be used to segment directly the acoustical image under study, the final result will be an image of a very low quality or directly wrong. For this reason, limits $L_{c_1}, \ldots, L_{c_{n-1}}$ and the estimated threshold T are combined to determine which region $c_1, \ldots, c_n$ contains the cell under test $x_{i,j}$. An estimator $\hat{L}_c$ is needed to obtain these limits. As it may be seen in Fig. 2, its inputs are the global histogram H_g and the different percentages $\%p_1, \ldots, \%p_{n-1}$. These percentages $\%p_1, \ldots, \%p_{n-1}$ are constant values representing an overall proportion of types of regions $c_1, \ldots, c_n$. They are established *a priori* from the observation of the global histogram, and this is why we called them region class percentages, depending on the acoustical data acquired by a particular sonar device features.

Fig. 5 shows in detail the pseudocode of the general framework for acoustical segmentation using OS-CFAR 2-D. This pseudocode contains all modifications to use OS-CFAR technique in the acoustic environment. The internal functions determine_limits $L_{c_1}, \ldots, L_{c_{n-1}}$ (see line 2 in Fig. 5), initialize H_p (see line 5 in Fig. 5), calculate_statistic_order x_k (see line 14 in Fig. 5), and calculate_alpha α_{OS} (see line 15 in Fig. 5) are described in the appendix.

The pseudocode input parameters are (see Fig. 5) acoustic image I of size $h \times w$ reference cells N and false alarm probability P_{fa}. The output represents a synthetic image O of size $h \times w$ that contains the segmentation of input image I. Besides, the pseudocode has different set constants: region classes $c_1, \ldots, c_n$ and global percentages $\%p_1, \ldots, \%p_{n-1}$ constant statistic order k used, and the image bit depth b of the digitized acoustical reverberation power. Finally, different auxiliary variables are needed for storage as: segmentation limits $L_{c_1}, \ldots, L_{c_{n-1}}$, partial kernel histogram H_p of size $b \times 1$, auxiliary v representing the digitized acoustical reverberation power for each position in image I, total number cells N_c, and value $x_{(k)}$. A set of basic steps can then be distinguished in the pseudocode process.

1) Determine_Limits $L_{c_1}, \ldots, L_{c_{n-1}}$: This function is in charge of estimating the segmentation limits $L_{c_1}, \ldots, L_{c_{n-1}}$ from a global histogram H_g (see line 2 in Fig. 5). The pseudocode of this function is detailed in the appendix.

2) Create Histogram H_p: In this step, the data structure to store the partial kernel histogram H_p (see line 3 in Fig. 5) is created and the memory needed for an array of size $b \times 1$ is reserved, where b denotes the image bit depth.

3) Initialize Histogram H_p: This function gives partial kernel histogram H_p its initial values (see line 5 in Fig. 5), an action that must be repeated for every row. The pseudocode of this function is detailed in the appendix. It can be further split into two substeps: 1) The kernel histogram H_p is initialized with zero values; 2) for every row, the window centered at the first pixel is initialized with the appropriate image values.

4) Update Histogram H_p: The kernel histogram H_p is updated while sliding through the image (see lines 7–12 in Fig. 5). The updating H_p requires to remove $2N+1$ values from the left column and to add $2N+1$ values from the right column. This step is detailed in Section III-B.

5) Calculate Number Cells N_c: The number of cells N_c depends on the number of reference cells N when the sliding window limits are within the limits of image I. In this case, the calculation leads to the equation $(2N+1)^2$ (see line 13 in Fig. 5). On the other hand, when the sliding window limits are out of the limits of image I, the calculation also depends on the current position in the image (*row* and *col*). For further details in this calculation, refer to [4].

6) Calculate_Statistic_Order $x_{(k)}$: The $x_{(k)}$ value is computed from the updated partial kernel histogram H_p by accumulating frequen-

```
Input:
    • Acoustic image I of size h x w
    • Reference cells N
    • False alarm probability P_fa
Output:
    • Segmentation image O of the same size as I
Constants:
    • Region classes c_1, ..., c_n
    • Regions class percentages %p_1, ..., %p_n-1
    • Constant statistic order k
    • Bit-depth b
Auxiliary:
    • Alpha multiplier α_OS
    • Segmentation limits L_c1, ..., L_cn-1
    • Partial kernel histogram H_p of size b × 1
    • Acoustical reverberation power value v
    • Total number of cells N_c
    • k-th element x_(k) of H_p
1  BEGIN
2    determine_limits L_c1, ..., L_cn-1
3    create_histogram H_p
4    FOR (row ← 1 to row <= h inc +1)
5      initialize H_p
6      FOR (col ← 1 to col <= w inc +1)
7        FOR (i ←−N to i <= N inc +1)
8          v ← I_(row+i,col−N−1)
9          H_p(v,1) ← H_p(v,1) − 1
10         v ← I_(row+i,col+N)
11         H_p(v,1) ← H_p(v,1) + 1
12       END FOR
13       N_c ← (2N + 1)^2
14       calculate_statistic_order x_(k)
15       calculate_alpha α_OS
16       T ← x_(k)α_OS
17       IF (T < L_c1) THEN
18         O_(row,col) ← c_1
19       ELSE IF (T > L_c1 AND T < L_c2) THEN
20         O_(row,col) ← c_2
21       ……"
22       ELSE
23         O_(row,col) ← c_n
24       END IF
25     END FOR
26   END FOR
27 END
```

Fig. 5. Pseudocode of the general framework for acoustical segmentation using OS-CFAR 2-D.

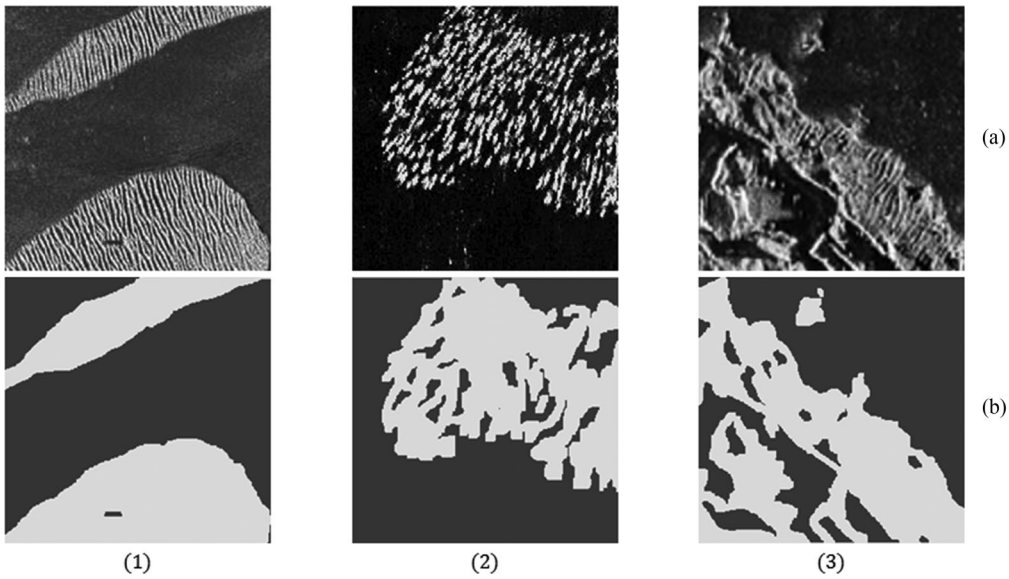

Fig. 6. Reference images to apply different approaches: (a) input sonar image and (b) manual segmentation by an expert.

cies from one extreme and stopping when this cumulative sum reaches the order statistics k (see line 14 in Fig. 5). The pseudocode of this function is detailed in the appendix.

7) Calculate_Alpha α_{OS}: This function calculates and extends alpha multiplier α_{OS} to real values using linear interpolation (see line 15 in Fig. 5). This step depends on false alarm probability P_{fa}, the number cells N_c, and order statistic k. The pseudocode of this function is detailed in the appendix.

8) Calculate Filtered Cell Value: The filtered cell value is calculated multiplying the value $x_{(k)}$ by alpha multiplier α_{OS} (see line 16 in Fig. 5).

9) To Segment in $c_1, \ldots, c_n$ Regions: The filtered cell value is compared to the limits $L_{c_1}, \ldots, L_{c_{n-1}}$ to segment a finite group of *n* regions $c_1, \ldots, c_n$ (see lines 17–24 in Fig. 5). Therefore, each pixel of output synthetic image *O* contains a class region.

IV. Experimental Results and Comparisons

This proposed framework for acoustical segmentation using OS-CFAR 2-D was developed originally with MATLAB and then it was ported to code written in C++, taking advantage of the data structure within OpenCV 2.3 [37]. The programming environment (IDE) was Nokia QtCreator for GNU/Linux implementation code C++. The framework was executed on a PC with a CPU 2.4 GHz Intel Core i7-3630, and 8-GB RAM memory, with Ubuntu 14.04 LTS (32 bits) operating system. This section describes three experiments: 1) quantitative and performance analyses comparing the proposed framework with AC, UDWT, MRF, ACA-CFAR 2-D methods; 2) qualitative analysis for pipeline detection; and 3) qualitative analysis for seafloor object detection.

A. Quantitative and Performance Analysis

Different sonar images from several websites [38], [39] were selected to perform a quantitative and performance comparison among different segmentation approaches. These websites contain acoustic image galleries for testing (see Fig. 6). The original images are shown in Fig. 6(a), while the manual segmentation by an expert of these images is shown in Fig. 6(b). The comparison (see Fig. 7 and Table I) is performed among the proposed framework [see Fig. 7(e)] and the following methods: AC [see Fig. 7(a)], UDWT [see Fig. 7(b)], ACA-CFAR 2-D [see Fig. 7(c)], and MRF [see Fig. 7(d)].

For this first experiment, a binary segmentation process is applied, which consists of separating acoustic highlight regions from the rest of the image. Three images were selected. They represent: sand waves for seafloor analysis [see Figs. 6(1) and 7(1)]; a school of fish for biological observation [see Figs. 6(2) and 7(2)]; and a sunken ship for underwater archaeology studies [see Figs. 6(3) and 7(3)]. These acoustical images were taken using an SSS device with a frequency of 600 kHz. The size of every image for these experiments was of 256 × 256 ($h \times w$) in a grayscale with a b image bit-depth per sample of 8 bits.

Results of the segmentation process are generally subjective and depend on its particular application. There is not a standard method to objectively compare the results obtained by different segmentation methods [40]. For this reason, this evaluation and comparison is performed using the manual segmentation by an expert provided by Celik and Tjahjadi [1] [see Fig. 6(b)]. The build process was performed manually, separating the studied objects on each image. However, a real ground truthing operation (direct observation) was not carried out.

Two quantitative measures are used to compare the different methods: 1) the proportion ρ of segmented images and 2) runtime in seconds. The measure ρ is employed for comparing the segmentation map (SM) with the manual segmentation by an expert (SM_{GT}):

$$\rho = 1 - \frac{\sum_{i=1}^{S_w} \sum_{j=1}^{S_a} \emptyset\left(\text{SM}_{\text{GT}}(i,j), \text{SM}(i,j)\right)}{h \times w} \tag{7}$$

where h and w represent the rows and columns number of acoustic image, respectively. Here, $\emptyset(a,b) = 1$ when $a = b$, and $\emptyset(a,b) = 0$ when $a \neq b$. When SM and SM_{GT} are the same, then ρ is 1, and ρ approaches 0 when the dissimilarity between SM and SM_{GT} increases.

Results obtained through the proposed framework were achieved setting the parameters for images (1) and (2) with $P_{fa} = 0.01$ and $N = 5$ offering the segmentation limits $L_{\text{highlight}} = 453$ and 183, respectively, and for image (3), a $P_{fa} = 0.02$ and $N = 5$ offering a segmentation limit $L_{\text{highlight}} = 269$.

Table I shows that the ACA-CFAR 2-D approach is more efficient in runtime than the other approaches. Furthermore, as concluded in [4], ACA-CFAR 2-D is a robust method to reduce the speckle noise

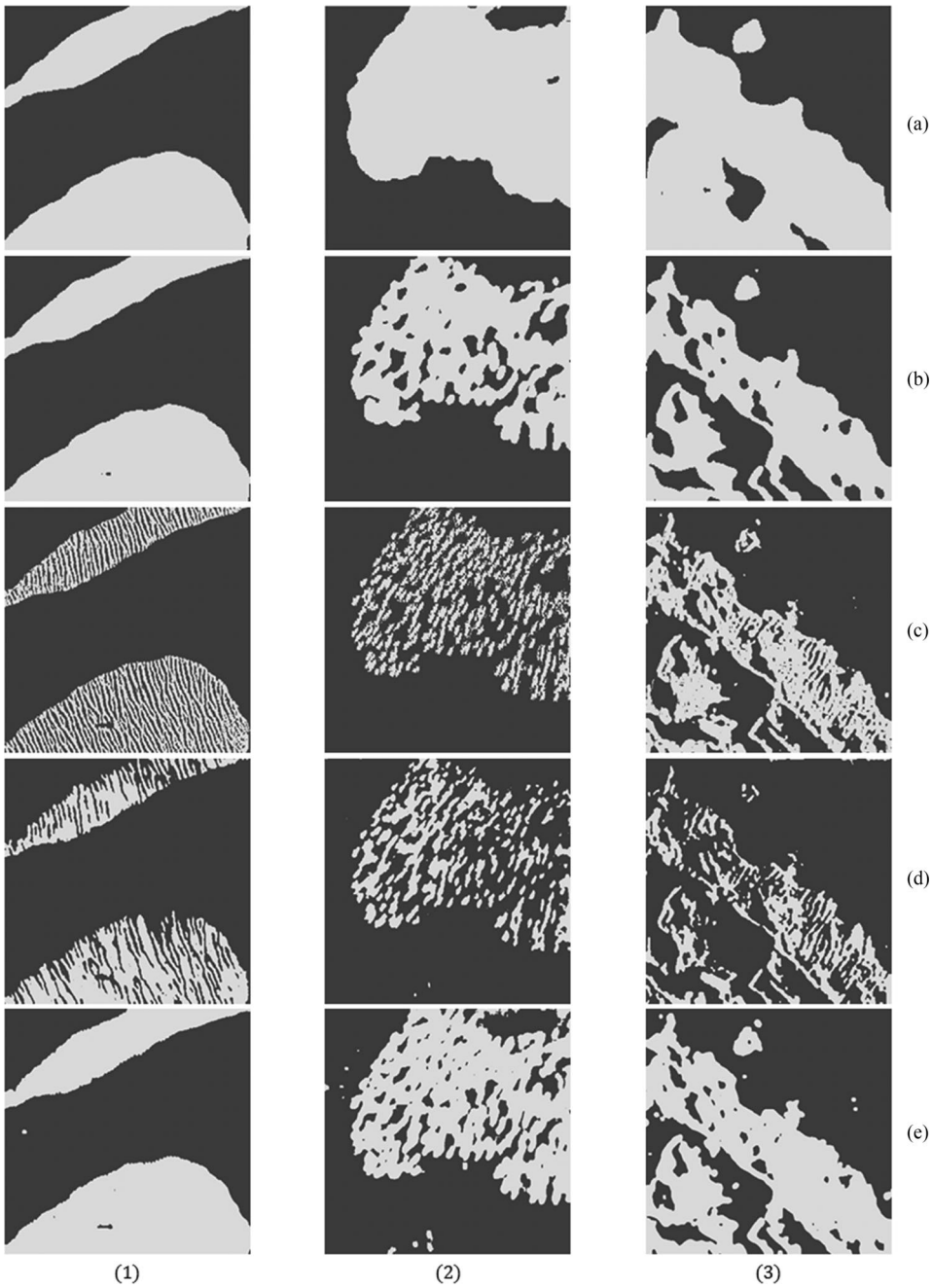

Fig. 7. Seafloor segmentation using the approaches: (a) AC; (b) UDWT; (c) ACA-CFAR 2-D; (d) MRF; and (e) proposed framework with OS-CFAR 2-D.

TABLE I
PERFORMANCE AND RUNTIME RESULTS OF DIFFERENT APPROACHES

Fig.		7.1	7.2	7.3
7(a) AC	ρ	97.77	87.52	84.69
	t[s]	309.18	288.92	322.78
7(b) UDWT	ρ	98.64	**92.94**	92.80
	t[s]	2.15	2.33	2.22
7(c) ACA-CFAR 2-D	ρ	82.08	80.50	85.57
	t[s]	**0.142**	**0.148**	**0.15**
7(d) MRF	ρ	84.08	73.59	72.59
	t[s]	4.76	2.65	4.28
7(e) OS-CFAR 2-D	ρ	**98.68**	91.02	**93.09**
	t[s]	2.17	2.34	2.25

and its implementation is extremely simple. These features make it especially interesting to be used in the perception system of an aquatic robot such as an autonomous underwater or an autonomous surface vehicle, which must make decisions in real time to provide efficient feedback to a dynamic mission replanner or an adaptive control of the robot, based on data acquired from sonar. On the other hand, the proposed framework and the UDWT approach performed a more precise segmentation than ACA-CFAR 2-D and AC with a similar runtime. Both approaches can be used for tasks that require precise results, such as seabed classification, marine geology, and underwater archaeology, among others. The MRF method required 9 iterations, distance $N = 2$ to the kernel center (neighborhood level), and 20% of highlight areas for the first initialization (these values have a significant impact on the rapidity of the convergence and on the quality of the final estimates

[17], [18]) to reach an optimum for the images in Fig. 7(1), (2), and (3), respectively. Its performance was the worse in this set of experiments with our parametrization.

The proposed framework using OS-CFAR 2-D presented the best performance regarding the measure ρ for Fig. 7(1) and (3) of Table I. An additional advantage of OS-CFAR 2-D was its simple implementation. This is because it does not require complex chain processes, such as the nested process of UDWT (wavelet transform, inter- and intraresolution implementation, principal component analysis, clustering, and among others), or the recursive iterations of MRF (which are unknown beforehand).

Even though we based our comparative analysis on the measure ρ proposed in [1], it may be argued that it is somehow subjective to evaluate each approach. It may be interesting to complement this analysis with an algorithmic complexity evaluation. In this sense, ACA-CFAR 2-D [4] exhibits an algorithmic complexity of $O(h \times w)$. When the image is square, complexity is then quadratic. The OS-CFAR 2-D algorithmic complexity depends on the sort method. In this paper, we used *Huang's* method [34], whose algorithmic complexity is $O(h \times w \times r)$, where r is the radius size of the sliding window.

B. Qualitative Analysis for Pipeline Detection

The first test of the framework proposed for pipe detection was performed using SSS images acquired in surveys in Salvador de Bahía, Brazil. For these surveys, an SSS *Starfish 450F* device (with chirped signal [430 kHz, 470 kHz]) of the Tritech company, Westhill, U.K., was used. The maximum range established was 50 m. The sonar was mounted on the hull (bow) of the boat survey using stainless steel support. The boat followed a pipeline, which was situated about 18 m in depth. The maximum range of the sonar was configured to stay between three or four times higher than the water depth. SSS sounding *beams* were run perpendicular to the line track of the boat. Data were acquired at 30° from nadir on both port and starboard side of the SSS. Also, the azimuthal angle was 1.7°. In these sonar images, the pipeline exhibits stronger backscattering than the seabed. Moreover, the sonar shadow formed after the pipeline is a very useful marker for this type of objects. The boat speed was less than 4.5 m/s for depths between 5 and 20 m and it was reduced to 1.5 or 2 m/s in deeper waters ($>$20 m), according the best practices of National Oceanic and Atmospheric Administration. This allowed us to have correct coverage from adjoining sonar acoustic *beams* in the form of SSS grayscale images. These images were saved in a binary map file format with 8 bits per pixel, i.e., pixel gray levels were between 0 and 255. In this experiment, the only possible geometrical corrections were slant-range correction and sound-speed correction that described in [9]. As we did not have any available inertial navigation unit during data collection, corrections to avoid roll, pitch, and yaw effects over the image could not be done. However, as this experimental evidence supports it, segmentation and then detection of the pipelines could be successfully done. This implies that the proposed methodology is robust enough to face practical applications.

The pipeline tracking was done in two sections: the first one was initiated at latitude $-12°51' \ 19.5''$ S and longitude $-38°32' \ 23.03''$ W, and concluded at latitude $-12°52' \ 23.28''$ S and longitude $-38°33' \ 48.48''$ W. About 50 500 beams of valid acoustic data were collected, yielding 101 images at 1000 $\times$ 500 pixels for testing the algorithms. The second section, started at latitude $-12°53' \ 33.04''$ S and longitude $-38°33' \ 48.14''$ W, and concluded at latitude $-12°52' \ 16.1''$ S and longitude $-38°31' \ 37.14''$ W, collecting 47 000 beams of acoustic data totaling 94 images of the same size the ones obtained for the first test stage.

Fig. 8 shows examples of SSS images (a) without further processing and the (b) results of having applied the proposed framework. The pipeline deployed on the seafloor is observed. Besides, these images have been cropped for better presentation.

Results obtained applying the proposed framework were achieved by setting the parameters for all images with $P_{fa} = 0.04, N = 3$, and the segmentation limits $L_{\text{highlight}} = 295$ for Fig. 8(1)–(3) and $L_{\text{highlight}} = 290$ for Fig. 8(4). P_{fa} was selected as lower as possible to avoid false alarms, N was selected according to the image resolution; in this case, it was a good tradeoff to select $N = 3$. Finally, the limits $L_{\text{highlight}}$ were selected in a trial-and-error sketch.

The pipelines in Fig. 8(1) and (3) were acquired from the right channel of the SSS device (starboard). On the other hand, the pipelines in Fig. 8(2) and (4) were acquired from the left channel (port). In Fig. 8(1)–(3), the pipeline is slightly curved and a lot of sediment has been accumulated which may have produced false detections. In Fig. 8(4), a straight and well-defined pipeline can be observed.

Based on navigation data, pipeline lies 20 m deep from the SSS acoustic device. At this depth, the shadow near the pipeline is not completely defined, and for this reason binary segmentation has to be performed (acoustic highlight and seafloor reverberation areas).

Segmentation results provided by this framework illustrate that pipeline objects detected show small gaps. This is due to the movement of the vehicle carrying the sonar device. Moreover, Fig. 8(2)–(4) shows small objects that could represent stones on the seafloor. One way to confirm this would be through direct observation in the detection point (latitude and longitude) where the object is located.

The second test of the proposed framework was carried out using SSS images acquired through an AUV (see Figs. 9–11). The AUV sailed to a depth of 5 m above the seafloor with a speed of 2 m/s. An Edgetech company, Ada, OK, SSS device was used for this test, also with a chirped signal.

Figs. 9 and 10 show a segmentation of three classes: highlight (white color), shadow (black color), and seafloor reverberation areas (gray color). The results obtained for Fig. 9 through the proposed framework were achieved setting the parameters with $P_{fa} = 0.04, N = 2$, and segmentation limits $L_{\text{shadow}} = 20$ and $L_{\text{highlight}} = 550$. Note that the values lower than 20 are considered as shadows, the values lower than 550 and greater or equal than 20 are considered as seafloor reverberation area, and values greater or equal than 550 are considered as highlight area.

Consider the underwater pipelines deployed on seafloor shown in Fig. 9. These presented images have been cropped for better presentation. Each image shows precisely a pipeline and its corresponding shadow. For all images, the pipelines were acquired from the right channel of the SSS device (starboard). In addition, useful inspection features can be observed: free span, rock dump, and reflective objects on the seafloor. The free span feature can be clearly observed in Fig. 9(2) where the shadow close to the pipeline is not completely defined. In other words, a seafloor acoustic reverberation area is between pipeline and shadow. From this feature, it can be inferred that the pipeline is not deployed on the seafloor and could collapse causing economic and environmental disaster. The most common method to solve this problem is known as rock dumping. This feature is observed in Fig. 9(1) and (2) where the pipeline is wider. Usually, rock dumping has to be examined to ensure stability.

Fig. 10 shows six images: (a) original image of a pipeline within a trench, acquired through the SSS *Edgetech* acoustic device; (b) original image plotted in 3-D (along track, across track, and backscattering), with SSS inherent speckle noise; (c) and (d) output detection threshold surface plotted in 2-D (along track, across track) and 3-D (along track, across track, and threshold), respectively, calculated according to the

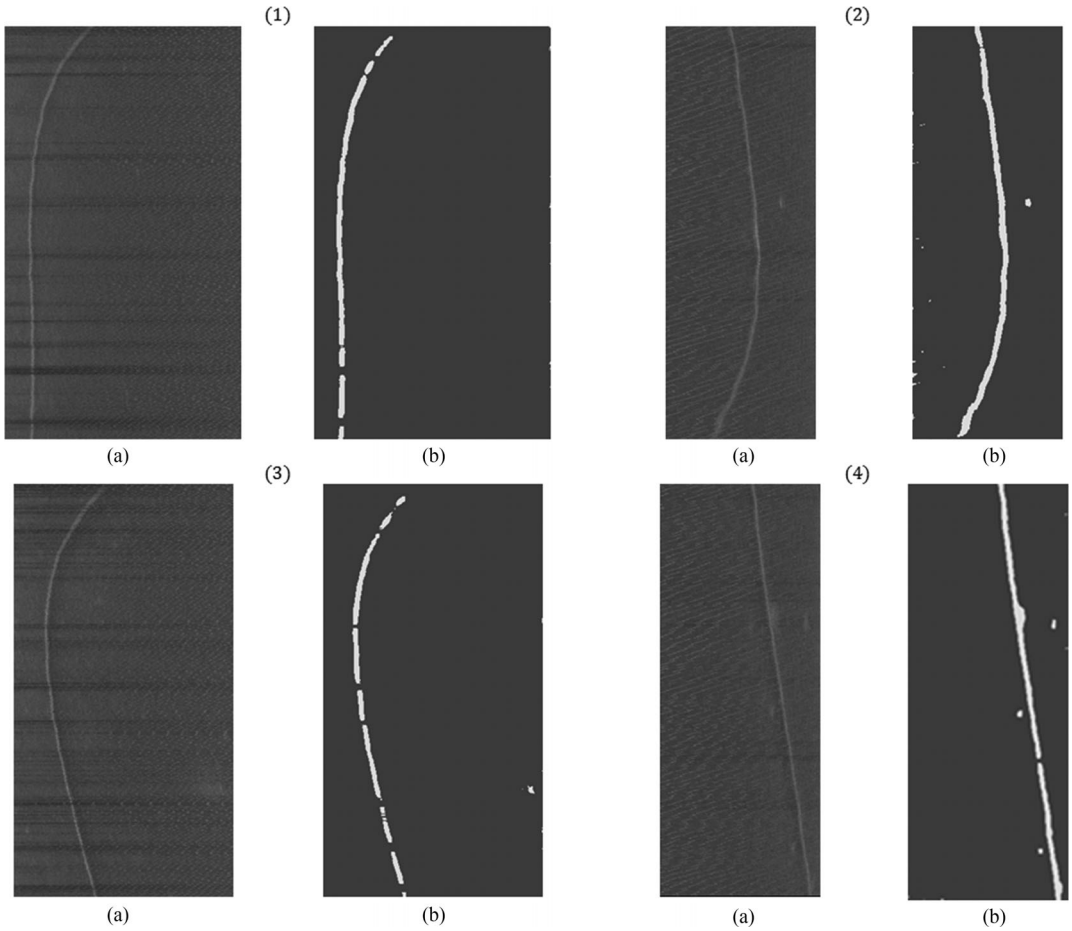

Fig. 8. Sonar image for pipes detection on seafloor (Starfish 450F device): (a) images without processing; (b) segmented images using our proposed framework with OS-CFAR 2-D.

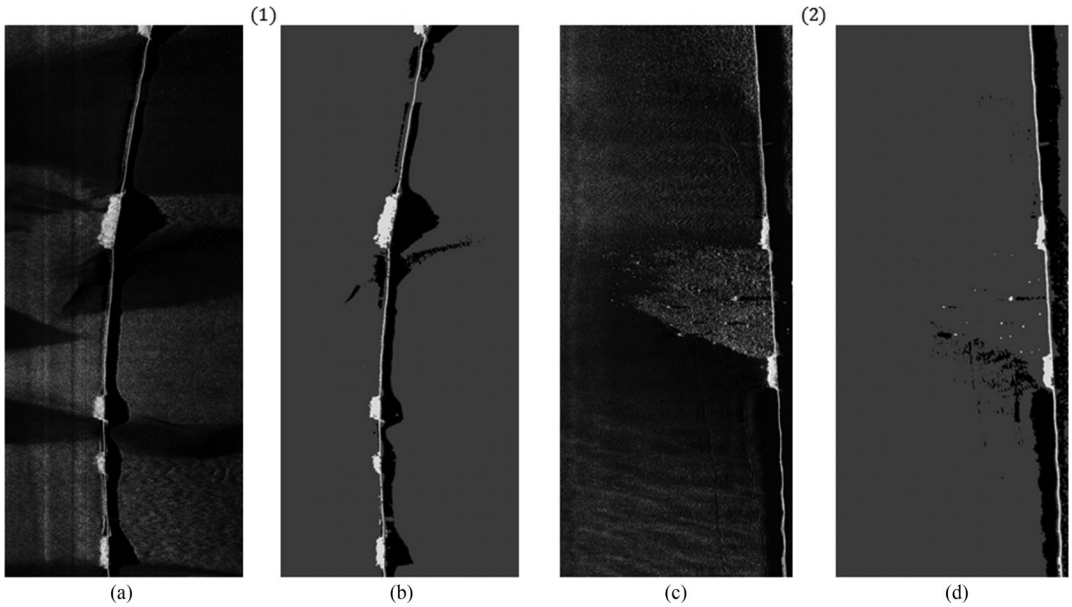

Fig. 9. Sonar image for pipes detection on seafloor (Edgetech device): (a) and (c) input sonar image; (b) and (d) segmented image using proposed framework with OS-CFAR 2-D.

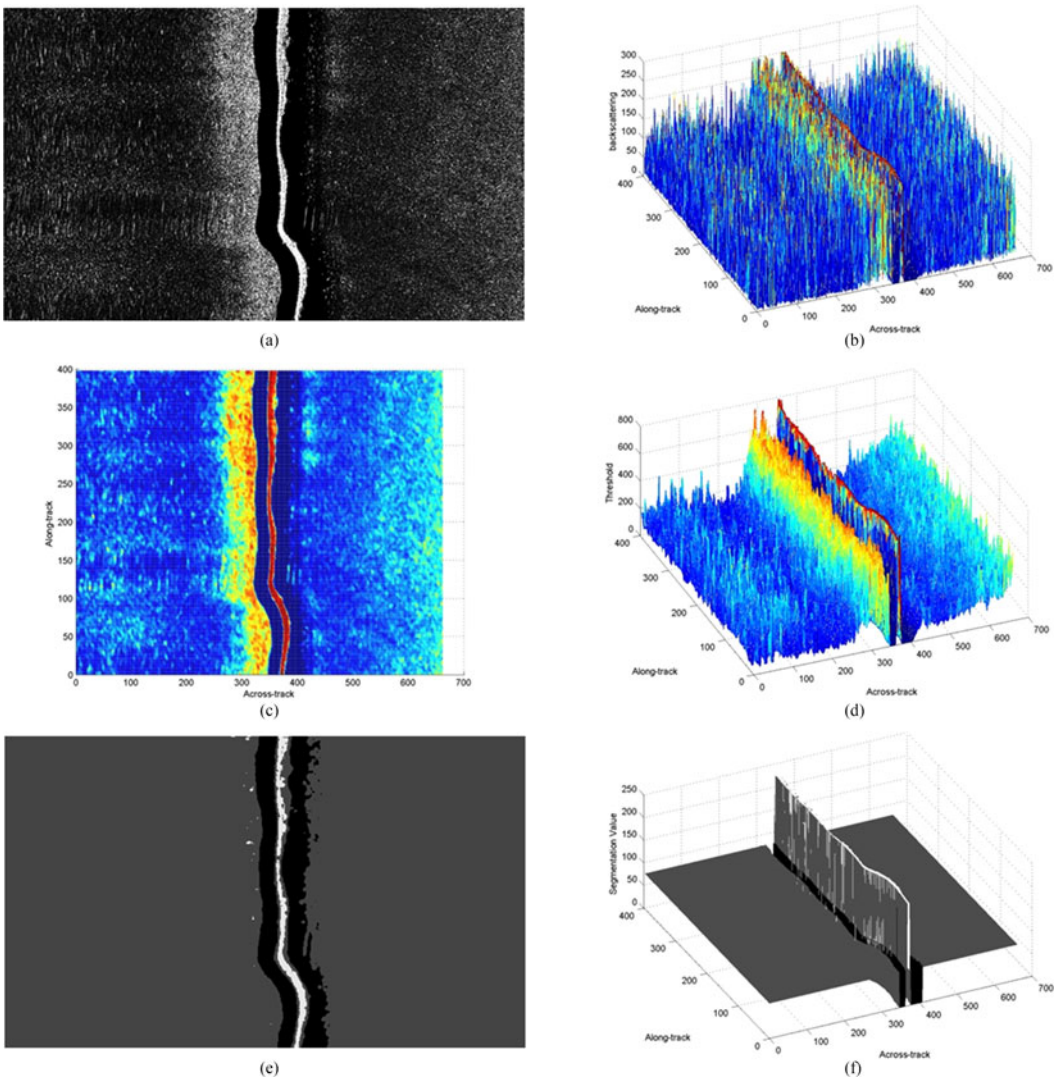

Fig. 10. Sonar image for pipes detection on seafloor (Edgetech device): (a) sonar image yielded by the SSS; (b) the original image of (a) plotted in 3-D where the speckle noise can be better appreciated; (c) output detection threshold plotted in 2-D after applying the OS-CFAR 2-D; (d) output detection threshold surface plotted in 3-D after applying the OS-CFAR 2-D; (e) segmented image using our proposed framework with OS-CFAR 2-D; and (f) segmented image plotted in 3-D using our proposed framework with OS-CFAR 2-D.

proposed framework; (e) segmentation process results using the proposed framework with setting the parameters $P_{fa} = 0.04$, $N = 2$, $L_{\text{shadow}} = 20$ and $L_{\text{highlight}} = 550$; and (f) segmented image plotted in 3-D (along track, across track, and segmentation value set) using our proposed framework with OS–CFAR 2-D. The particular feature of the pipeline within a trench is determined because the acoustic shadow lies on both sides of the pipeline. The effective detection is done in Fig. 10(e). Note also in Fig. 10(d) that the filtered surface is decreasing the original speckle noise of the image. This noise is reduced due to the use of OS-CFAR 2-D approach.

Fig. 11 shows a generalization to the segmentation in *n* classes, with $n = 4$. This segmentation allows us to separate among four classes: highlight (white color), shadow (black color), strong seafloor reverberation (light gray color), and lower seafloor reverberation areas (dark gray color). The results obtained for Fig. 11 by means of the proposed framework were achieved setting the parameters as $P_{fa} = 0.04$, $N = 2$, $L_{\text{shadow}} = 20$, $L_{\text{reverberation}} = 150$, and $L_{\text{highlight}} = 550$. Note that the values less than 20 are considered as shadows, the values between less than 150 and greater or equal than 20 are considered

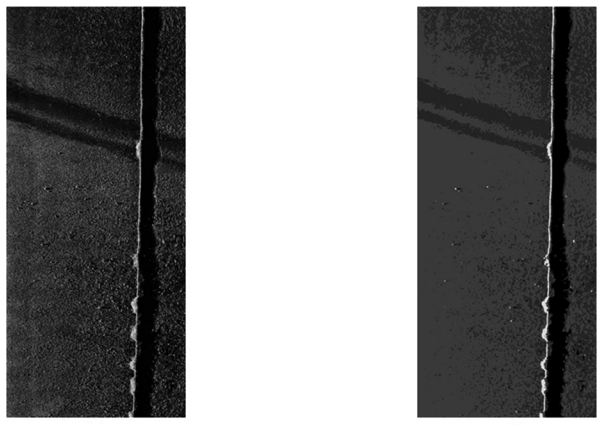

Fig. 11. Sonar image for pipes detection on seafloor (Edgetech device): (a) input sonar image; (b) segmented image using proposed framework with OS-CFAR 2-D.

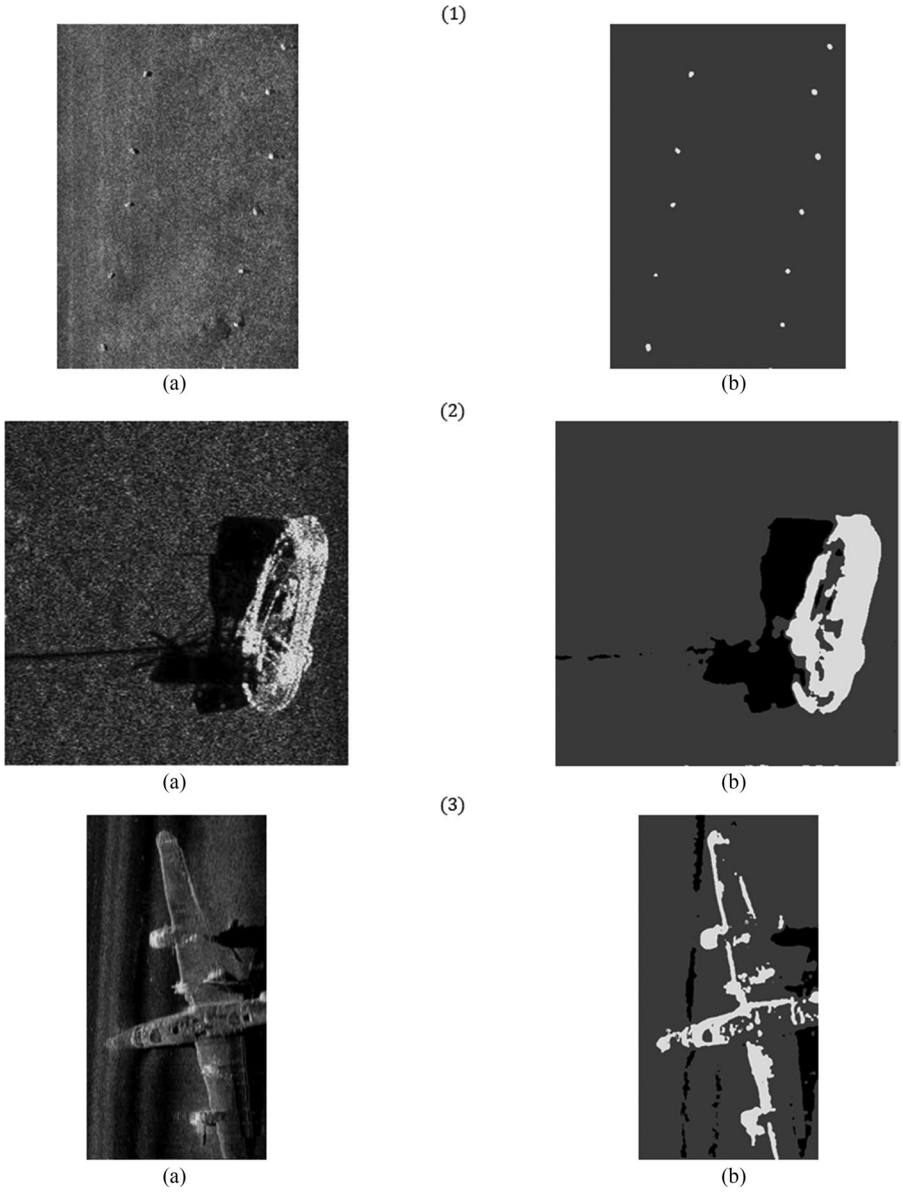

Fig. 12. Sonar image of different seefloor objects: (1) lobster traps; (2) sunken ship; and (3) sunken airplane. (a) Input sonar image and (b) segmented image using proposed framework with OS-CFAR 2-D.

as lower seafloor reverberation area, the values smaller than 550 and greater or equal than 150 are considered as strong seafloor reverberation area, and the values greater or equal than 550 are considered highlight area.

C. Qualitative Analysis for Seafloor Object Detection

Fig. 12 shows three examples of different issues using the proposed framework. Fig. 12(1) shows the detection of small lobster cages deployed on the seafloor. This image was selected from website [41] and it was acquired by a *Klein System 3900* SSS acoustic device. These small lobsters cages are effectively detected through the proposed framework. The parameters used for this binary segmentation are $P_{fa} = 0.04$, $N = 2$, and $L_{\text{highlight}} = 470$.

Fig. 12(2) shows a detection of a sunken ship located on Lake Washington. The image was acquired by Marine Sonic Technology, Yorktown, VA, at a frequency of 600 kHz and at a maximum range of 50 m [38]. Similarly, Fig. 12(3) shows an image of a sunken plane (Consolidated PB4Y2 Privateer) acquired for the same company. This image was taken at a frequency of 600 kHz at a maximum range of 20 m. These images are of special interest particularly for rescue or archaeological studies. The results obtained for Fig. 12(2), (3) were achieved setting the parameters with $P_{fa} = 0.02$, $N = 4$, $L_{\text{shadow}} = 140$, $L_{\text{highlight}} = 400$ and with $P_{fa} = 0.04$, $N = 3$, $L_{\text{shadow}} = 10$, $L_{\text{highlight}} = 300$, respectively.

A summary of the selected parameters for every segmentation obtained from experimental data (see Figs. 7–12) is given in Table II. N_c and α_{OS} are indirect parameters computed from the remaining ones. The probability of false alarm P_{fa} and the number of reference cells

TABLE II
SUMMARY TABLE OF PARAMETERS USED

Fig.	P_{fa}	N	N_c	k	α_{OS}
7(1)	0.01	5	121	90	3669
7(2)					
7(3)	0.02				2986
8(1)	0.04	3	49	36	2.948
8(2)					
8(3)					
8(4)					
9(1)		2	25	18	
9(2)					
10					
11					
12(1)					
12(2)	0.02	4	81	60	2986
12(3)	0.04	3	49	36	2.948

(N) were chosen from a trial-and-error sketch based on the detection and segmentation performances.

V. CONCLUSION

This paper presented a general framework for segmenting images obtained through different SSS acoustic devices. The framework was experimentally and successfully tested to separate up to four classes ($n = 4$). Its application was demonstrated through different tests that focused on current problems. OS-CFAR represents one of the most used techniques in radar technology for moving object detection in real time. This paper provides another proof about the utility of shifting radar technology to sonar technology. It also provides a sound experimental comparison between OS-CFAR 2-D as a segmentation technique on one side and other methods such as UDTW, AC, MRF, and ACA-CFAR 2-D on the other side. This allows stating the robustness of OS-CFAR 2-D regarding its accuracy and ability to separate among *n* classes. Therefore, it may be concluded that it is a useful technique for soil taxonomy, underwater archeology, and dock works among other applications. In addition, this approach has several advantages. For instance, it needs few parameters to be set: reference cells, false alarm probability, and region class percentages. They were tuned from a previous analysis of the acoustical image obtained by the particular sonar, as explained in previous paragraphs. Another benefit is that OS-CFAR 2-D is easy to implement. Its computational complexity only depends on the mean sorting method.

Finally, the runtime comparison that was proposed in [1] is somehow subjective, in our opinion, to evaluate each approach. Instead, it would be more precise if complemented with an algorithmic complexity evaluation. For instance, ACA-CFAR 2-D [4] exhibits an algorithmic complexity of $O(h \times w)$. When the image is square, complexity is quadratic. The OS-CFAR 2-D algorithmic complexity depends on the sort method. In this paper, we used Huang's method [34], whose algorithmic complexity is $O(h \times w \times r)$, where r is the radius size of the sliding window.

APPENDIX

This appendix contains the internal functions that implement the pseudocode of general framework for acoustical segmentation using OS-CFAR 2-D. Among them are: determine_limits $L_{c_1}, \ldots, L_{c_{n-1}}$ (see Fig. I1), Initialize H_p (see Fig. I2), calculate_statistic_order value $x_{(k)}$ (see Fig. I3), and calculate_alpha α_{OS} (see Fig. I4).

A. Determine_Limits $L_{c_1}, \ldots, L_{c_{n-1}}$

```
Auxiliaries:
    • Total histogram H_g of size b × 1
    • Accumulated percentage %p_acc
    • Acoustical reverberation power value v
    • Sum of Acoustical reverberation power sum
    • If the limit is founded found
2.1  BEGIN
2.2    create histogram H_g
2.3    FOR (i ← 0 to i <= b inc +1)
2.4      H_g(i,1) ← 0
2.5    END FOR
2.6    FOR (row ← 1 to row <= h inc +1)
2.7      FOR (col ← 1 to col <= w inc +1)
2.8        v ← I(row,col)
2.9        H_g(v,1) ← H_g(v,1) + 1
2.10     END FOR
2.11   END FOR
2.12   %p_acc ← 0
2.13   FOR (j ← 1 to j <= n inc +1)
2.14     %p_acc ← %p_acc + %p_j
2.15     sum ← 0
2.16     found ← FALSE
2.17     i ← 0
2.18     WHILE (i <= b AND NOT found) DO
2.19       sum ← sum + H_g(i,1)
2.20       IF (%p_acc ≥ (sum ×100 / h×w)) THEN
2.21         L_cj ← i
2.22         found ← TRUE
2.23       END IF
2.24       i ← i+1
2.25     END WHILE
2.26   END FOR
2.27   Return ← L_c1, …, L_cn-1
2.28 END
```

Fig. I1. Pseudocode for determine_limits $L_{c_1}, \ldots, L_{c_{n-1}}$.

B. Initialize H_p

```
Auxiliaries:
    • Acoustical reverberation power value v
5.1  BEGIN
5.2    FOR (i ← 0 to i < b inc +1)
5.3      H_p(i,1) ← 0
5.4    END FOR
5.5    FOR (i ← −N to i <= N inc +1)
5.6      FOR (j ← −N to j < N inc +1)
5.7        v ← I(row+i,1+j)
5.8        H_p(v,1) ← H_p(v,1) + 1
5.9      END FOR
5.10   END FOR
5.11 END
```

Fig. I2. Pseudocode for initialize H_p.

C. Calculate_Statistic_Order $x_{(k)}$

```
Auxiliaries:
    • Accumulator of Acoustical reverberation power acc
14.1  BEGIN
14.2    acc ← 0
14.3    FOR (i←0 to (i< b) AND (acc<N_c × k) inc+1)
14.4      acc ← acc + H_p(i,1)
14.5      x_(k) ← i
14.6    END
14.7  Return ← x_(k)
14.8  END
```

Fig. I3. Pseudocode for calculate_statistic_order value x_k.

D. Calculate_Alpha α_{OS}

```
Auxiliaries:
    • False alarm probability p_fa_0, p_fa_1
    • If the α_OS is founded found
15.1  BEGIN
15.2    found ← FALSE
15.3    i ←0
15.4    p_fa_0 ← = N_c!(i+N_c−k)! / (N_c−k)!(i+N_c)!
15.5    WHILE (NOT found) DO
15.6      i ← i + 1
15.7      p_fa_1 ← = N_c!(i+N_c−k)! / (N_c−k)!(i+N_c)!
15.8      IF (P_fa ≤ p_fa_0 AND P_fa ≥ p_fa_1) THEN
15.9        found ← TRUE
15.10         α_OS* ← (i − 1) + (P_fa − p_fa_0) / (p_fa_1 − p_fa_0)
15.11     END IF
15.12     p_fa_0 ← p_fa_1
15.13   END WHILE
15.14   Return ← α_OS
15.15 END
```

Fig. I4. Pseudocode for calculate_alpha α_{OS}.

REFERENCES

[1] T. Celik and T. Tjahjadi, "A novel method for sidescan sonar image segmentation," *IEEE J. Ocean. Eng.*, vol. 36, no. 2, pp. 186–194, Apr. 2011.

[2] X. Lurton, *An Introduction to Underwater Acoustics. Principles and Applications* (Springer Praxis Books in Geophysical Sciences). Berlin, Germany: Springer-Verlag, 2002, ch. 7 and 8.

[3] P. Chapple, "Automated detection and classification in high-resolution sonar imagery for autonomous underwater vehicle operations," Maritime Oper. Div. Defense Sci. Technol. Org., Edinburgh, SA, Australia, Rep. DSTO-GD-0537, 2008.

[4] G. G. Acosta and S. A. Villar, "Accumulated CA–CFAR process in 2-D for online object detection from sidescan sonar data," *IEEE J. Ocean. Eng.*, vol. 40, no. 3, pp. 558–569, Jul. 2015.

[5] P. Blondel, *The Handbook of Sidescan Sonar*. Berlin, Germany: Springer-Verlag, 2009, ch. 3 and 4.

[6] S. Reed, Y. Petillot, and J. Bell, "An automatic approach to the detection and extraction of mine features in sidescan sonar," *IEEE J. Ocean. Eng.*, vol. 28, no. 1, pp. 90–105, Jan. 2003.

[7] S. Reed, Y. Petillot, and J. Bell, "Automated approach to classification of mine-like objects in sidescan sonar using highlight and shadow information," *Proc. Inst. Elect. Eng. Radar, Sonar Navig.*, vol. 151, no. 1, pp. 48–56, Feb. 2004.

[8] S. A. Villar, A. L. Sousa, A. Rozenfeld, and G. G. Acosta, "Pipeline detection system in acoustic images utilizing CA-CFAR," presented at the OCEANS 2013 MTS/IEEE, San Diego, CA, USA, 2013.

[9] S. A. Villar, G. G. Acosta, A. L. Sousa, and A. Rozenfeld, "Evaluation of an efficient approach for target tracking from acoustic imagery for the perception system of an autonomous underwater vehicle," *Int. J. Adv. Robot. Syst.*, vol. 11, no. 24, pp. 1–13, 2013.

[10] I. Ishøy *et al.*, "New challenges for AUTOTRACKER," presented at the Unmanned Underwater Vehicle Showcase, Southampton, U.K., 2002.

[11] X. F. Ye, Z. H. Zhang, P. X. Liu, and H. L. Guan, "Sonar image segmentation based on GMRF and level-set models," *Ocean Eng.*, vol. 37, no. 10, pp. 891–901, 2010.

[12] R. C. Gonzalez and R. E. Woods, *Digital Image Processing*. 2nd ed. Upper Saddle River, NJ, USA: Prentice-Hall, 2001, ch. 5.

[13] S. Reed, I. Tena Ruiz, C. Capus, and Y. Petillot, "The fusion of large scale classified side-scan sonar image mosaics," *IEEE Trans. Image Process.*, vol. 15, no. 7, pp. 2049–2060, Jul. 2006.

[14] D. P. Williams, "Bayesian data fusion of multiview synthetic aperture sonar imagery for seabed classification," *IEEE Trans. Image Process.*, vol. 18, no. 6, pp. 1239–1254, Jun. 2009.

[15] I. Karoui, R. Fablet, J. M. Boucher, and J. M. Augustin, "Seabed segmentation using optimized statistics of sonar textures," *IEEE Trans. Geosci. Remote Sens.*, vol. 47, no. 6, pp. 1621–1631, Jun. 2009.

[16] D. R. Carmichael, L. M. Linnett, S. J. Clarke, and B. R. Calder, "Seabed classification through multifractal analysis of sidescan sonar imagery," *Proc. Inst. Elect. Eng. Radar, Sonar Navig.*, vol. 143, no. 3, p. 140, Jun. 1996.

[17] M. Mignotte, C. Collet, P. Pérez, and P. Bouthemy, "Three-class markovian segmentation of high-resolution sonar images," *Comput. Vis. Image Underst.*, vol. 76, no. 3, pp. 191–204, 1999.

[18] M. Mignotte, C. Collet, P. Perez, and P. Bouthemy, "Sonar image segmentation using an unsupervised hierarchical MRF model," *IEEE Trans. Image Process.*, vol. 9, no. 7, pp. 1216–1231, Jul. 2000.

[19] G. R. Cutter, Y. Rzhanov, and L. A. Mayer, "Automated segmentation of seafloor bathymetry from multibeam echosounder data using local fourier histogram texture features," *J. Exp. Marine Biol. Ecol.*, vol. 285/286, pp. 355–370, 2003.

[20] M. Lianantonakis and Y. R. Petillot, "Sidescan sonar segmentation using texture descriptors and active contours," *IEEE J. Ocean. Eng.*, vol. 32, no. 3, pp. 744–752, Jul. 2007.

[21] J. L. Starck, J. Fadili, and F. Murtagh, "The undecimated wavelet decomposition and its reconstruction," *IEEE Trans. Image Process.*, vol. 16, no. 2, pp. 297–309, Feb. 2007.

[22] S. A. Villar, A. Rozenfeld, G. G. Acosta, R. Prados, and R. Garcia Campos, "Mosaic construction from side-scan Sonar: A comparison of two approaches for beam interpolation," presented at the IEEE/OES Acoustics in Underwater Geosciences Symp., Universidade Federal Fluminense, Université Libre de Bruxelles Rio de Janeiro-Brasil, Rio de Janeiro, Brazil, 2015.

[23] M. A. Richards, *Fundamental of Radar Signal Processing*. New York, NY, USA: McGraw-Hill, 2005, ch. 7.

[24] P. P. Gandhi and S. A. Kassam, "Analysis of CFAR processors in homogeneous background," *IEEE Trans. Aerosp. Electron. Syst.*, vol. 24, no. 4, pp. 427–445, Jul. 1988.

[25] H. Rohling, "Radar CFAR thresholding in clutter and multiple target situations," *IEEE Trans. Aerosp. Electron. Syst.*, vol. AES-19, no. 4, pp. 608–620, Jul. 1983.

[26] S. Blake, "OS-CFAR theory for multiple targets and nonuniform clutter," *IEEE Trans. Aerosp. Electron. Syst.*, vol. AES-24, no. 6, pp. 785–790, Nov. 1988.

[27] C. de Moustier, "OS-CFAR detection of targets in the water column and on the seafloor with a multibeam echosounder," in *Proc. MTS/IEEE OCEANS*, 2013.

[28] N. Levanon, *Radar Principles*. New York, NY, USA: Wiley, 1988, ch. 5 and 6.

[29] F. E. Nathanson, J. P. Reilly, and M. N. Cohen, *Radar Design Principles*, 2nd ed. New York, NY, USA: McGraw-Hill, 1991, ch. 4.

[30] P. Cervenka, C. Moustier, and P. F. Lonsdale, "Geometric corrections on sidescan sonar images based on bathymetry. Application with SeaMARC II and sea beam data," *Marine Geophys. Res.*, vol. 16, no. 5, pp. 365–383, 1994.

[31] D. T. Cobra, A. V. Oppenheim, and J. S. Jaffe, "Geometric distortions in side-scan sonar images: A procedure for their estimation and correction," *IEEE J. Ocean. Eng.*, vol. 17, no. 3, pp. 252–268, Jul. 1992.

[32] M. Kronauge and H. Rohling, "Fast two-dimensional CFAR Procedure," *IEEE Trans. Aerosp. Electron. Syst.*, vol. 49, no. 3, pp. 1817–1823, Jul. 2013.
[33] M. Juhola, J. Katajainen, and T. Raita, "Comparison of algorithms for standard median filtering," *IEEE Trans. Signal Process.*, vol. 39, no. 1, pp. 204–208, Jan. 1991.
[34] T. Huang, G. Yang, and G. Tang, "A fast two-dimensional median filtering algorithm," *IEEE Trans. Acoust., Speech, Signal Process.*, vol. 27, no. 2, pp. 13–18, Feb. 1979.
[35] J. Tukey, *Exploratory Data Analysis*. Menlo Park, CA, USA: Addison-Wesley, 1977, ch. 7.
[36] G. R. Arce, *Nonlinear Signal Processing: A Statistical Approach*. Hoboken, NJ, USA: Wiley, 2005, ch. 6.
[37] G. Bradski and A. Kaehler, *Learning OpenCV: Computer Vision With the OpenCV Library*, 1st ed. Sebastopol, CA, USA: O'Reilly Media, 2008, ch. 3, 4, and 5.
[38] [Online]. Available: http://www.marinesonic.us/
[39] [Online]. Available: http://www.edgetech.com/
[40] W. K. Pratt, *Digital Image Processing: PIKS Inside*, 3rd ed. Hoboken, NJ, USA: Wiley, 2001, ch. 17.
[41] [Online]. Available: http://www.l-3mps.com/

Sebastián A. Villar (M'xx) received the Graduate degree in systems engineering from Exact Sciences Faculty, the MBA degree from Economic Science Faculty, and the Ph.D. degree in engineering from Engineering Faculty, all faculties in the National Buenos Aires Province Centre University (UNCPBA), Tandil, Argentina, in 2009, 2011, and 2014, respectively.

He is a Researcher of the Argentinean National Research Council with a scholarship, working in Engineering Group INTELYMEC, UNCPBA.

Mariano De Paula received the Graduate degree in industrial engineering from the Engineering Faculty, National Buenos Aires Province Centre University (UNCPBA), Tandil, Argentina, in 2007, and the Ph.D. degree in engineering from National Technological University, Buenos Aires, Argentina, in 2013.

Since 2015, he has been a Researcher of the Argentinean National Research Council, working in Engineering Group INTELYMEC, UNCPBA.

Franco J. Solari received the Graduate degree in physics and chemistry from the Engineering Faculty, Universidad Nacional del Centro de la Provincia de Buenos Aires (UNCPBA), Tandil, Argentina, in 2011, where since 2013, he has been working toward the Ph.D. degree.

He currently has a scholarship of the Argentinean National Research Council, working in the Research & Development Group "INTELYMEC" at the Engineering Faculty, UNCPBA. His research interests include artificial neural networks and SLAM techniques.

Gerardo G. Acosta (SM'01) received the Engineering degree in electronics from the National University of La Plata, La Plata, Argentina, in 1988, and the Ph.D. degree in computer science from the University of Valladolid, Valladolid, Spain, in 1995.

He is currently a Full Professor in control systems (electronic area) in the Engineering Faculty at the National Buenos Aires Province Centre University (UNCPBA), Tandil, Argentina. He is also a Researcher of the Argentinean National Research Council (CONICET), since 1997, and the Director of the Research & Development Group "INTELYMEC," CIFICEN CONICET-UNCPBA. His working interests comprise the use of computational intelligence in automatic control, particularly intelligent control techniques in terrestrial and underwater robotics. He has more than 150 publications and two copyrights in this and related fields.

Dr. Acosta was the Chairman of the IEEE Computational Intelligence Society Argentinean Chapter (2007–2008), received the 2010 Outstanding Chapter Award from CIS, and is the current Chairman of the IEEE Oceanic Engineering Society Argentinean Chapter, being one of its founders. He was also a Member of the Administrative Committee of the IEEE OES (2015–2016). He has been the Research Leader of more than ten R+D projects, funded by the Argentinean Government, the Spanish Government, and the European Union. He has been invited as a Professor of Ph.D. programs in Argentina and Spain. He is the present Director of the Ph.D. program at the Engineering Faculty, UNCPBA, and serve as a Reviewer and Member of the scientific committee of several national and international journals and conferences.